ADVANCED ENERGY MATERIALS
www.advenergymat.de

Understanding the Rate Capability of High-Energy-Density Li-Rich Layered $Li_{1.2}Ni_{0.15}Co_{0.1}Mn_{0.55}O_2$ Cathode Materials

Xiqian Yu, Yingchun Lyu, Lin Gu, Huiming Wu, Seong-Min Bak, Yongning Zhou, Khalil Amine, Steven N. Ehrlich, Hong Li, Kyung-Wan Nam,* and Xiao-Qing Yang**

The high-energy-density, Li-rich layered materials, i.e., $xLiMO_2(1-x)Li_2MnO_3$, are promising candidate cathode materials for electric energy storage in plug-in hybrid electric vehicles (PHEVs) and electric vehicles (EVs). The relatively low rate capability is one of the major problems that need to be resolved for these materials. To gain insight into the key factors that limit the rate capability, in situ X-ray absorption spectroscopy (XAS) and X-ray diffraction (XRD) studies of the cathode material, $Li_{1.2}Ni_{0.15}Co_{0.1}Mn_{0.55}O_2$ [$0.5Li(Ni_{0.375}Co_{0.25}Mn_{0.375})O_2 \cdot 0.5Li_2MnO_3$], are carried out. The partial capacity contributed by different structural components and transition metal elements is elucidated and correlated with local structure changes. The characteristic reaction kinetics for each element are identified using a novel time-resolved XAS technique. Direct experimental evidence is obtained showing that Mn sites have much poorer reaction kinetics both before and after the initial activation of Li_2MnO_3, compared to Ni and Co. These results indicate that Li_2MnO_3 may be the key component that limits the rate capability of Li-rich layered materials and provide guidance for designing Li-rich layered materials with the desired balance of energy density and rate capability for different applications.

1. Introduction

Lithium-ion batteries are considered to be one of the best candidates for hybrid electric vehicle (HEV) and plug-in hybrid electric vehicle (PHEV) applications. Among the commercially available cathode materials for Li-ion batteries, the 4 V spinel $LiMn_2O_4$ and 3.4 V olivine $LiFePO_4$ have drawn lots of attention due to their excellent cyclic performance, environmentally friendly nature, and low cost. Unfortunately, both $LiMn_2O_4$ and $LiFePO_4$ have low energy densities due to the low capacity for the former and the low operating voltage for the later. Recently, Li-rich layered oxides (represented by the chemical formula: $xLiMO_2(1-x)Li_2MnO_3$, where M represents a transition metal ion) are becoming more appealing as they exhibit high capacities over 250 mAh g^{-1} with high operating voltage (>3.5 V vs. Li/Li^+ on average).[1–8] To utilize the Li-rich layered oxides as electrode materials, extensive studies have been carried out over the past several years. One very interesting point for this composite material is the observation of a 4.5 V voltage plateau when charged (delithiation) in the first cycle, which is responsible for the extra high capacity for this type of material.[1–8] The origin of the extra capacity obtained in the initial high voltage region has been attributed to several possible causes: 1) Enhanced reactivity of Li_2MnO_3 structure regions. The irreversible loss of oxygen from the lattice,[2,6,9–11] formation of oxygen vacancies,[6,12–14] or partially oxidized oxygen anions[15,16] have been suggested to explain the charge compensation mechanism during the delithiation process in the high voltage plateau region. 2) The surface reaction through electrode/electrolyte reduction and/or hydrogen exchange.[5,9,17] 3) Oxidation of Mn^{4+} to Mn^{5+} is still one of the explanations that cannot be ruled out.[15,18] The charge compensation mechanism during the initial charge and the successive cycling process is not clearly understood.

Another very important issue from the application point of view is how to improve the relatively poor rate capability of the Li-rich layered materials. The solid electrolyte interface (SEI) layer formed on the cathode surface has been proposed to be one of the major reasons for the poor rate performance.[19,20] However, the rate capability was not significantly improved, even when the SEI on the surface was absent. Recently, Xu et al. proposed that the poor rate capability may be caused by the surface phase formed after the initial delithiation.[21] Although the formation of the SEI film or surface phase could slow down the kinetics of the lithium extraction/insertion in the surface region, the transport behavior in the bulk phase may also be important for the rate capability.[22,23] There are two important factors that affect the bulk transport properties: the structural

Dr. X. Q. Yu, Dr. S.-M. Bak, Dr. Y. N. Zhou, Dr. S. N. Ehrlich, Dr. K.-W. Nam, Dr. X.-Q. Yang
Chemistry Department
Brookhaven National Laboratory
Upton, NY, 11973, USA
E-mail: knam@bnl.gov; xyang@bnl.gov
Y. C. Lyu, Prof. L. Gu, Prof. H. Li
Beijing National Laboratory for Condensed Matter Physics
Institute of Physics
Chinese Academy of Sciences
Beijing, 100190, China
E-mail: hli@iphy.ac.cn
Dr. H. M. Wu, Dr. K. Amine
Chemical Sciences and Engineering Division
Argonne National Laboratory
Argonne, IL, 60439, USA

DOI: 10.1002/aenm.201300950

factor and the elemental factor. The structural factor considers the different reaction rates between the $LiMO_2$ and Li_2MnO_3 components. Although the poor electrochemical activity of the Li_2MnO_3 component,[24–26] can be enhanced significantly in the composite structure compared to that in the non-composite structure due to an unclear synergy effect, experimental results distinguishing the kinetic properties of each component in the composite would be very helpful for understanding the fundamentals of the kinetic properties. For the elemental factor, the charge transfer rate of each individual transition metal element (Ni, Co, and Mn), as well as the local structural changes near each of them are very important, particularly for Mn, which has at least two different structural environments ($LiMO_2$ and Li_2MnO_3). Therefore, an in-depth understanding with elemental selectivity for the delithiation kinetics that distinguishes the $LiMnO_2$ and Li_2MnO_3 components in bulk will provide valuable guidance for the optimization of Li-rich layered materials with improved rate capability.

The motivation of this work is to understand the rate capability of Li-rich layered materials and determine its structural origins. Due to the structural complexity of Li-rich layered materials (two components: $LiMO_2$, Li_2MnO_3, and multiple elements: Ni, Co, Mn), a combination of the X-ray diffraction (XRD), X-ray absorption spectroscopy (XAS), and galvanostatic intermittent titration technique (GITT) techniques were used to determine and differentiate the contributions to the capacity from each component and element. Then, a novel time-resolved XAS technique was applied to study the reaction kinetics of different components and elements.[27] The results show that Mn sites have poor reaction kinetics compared with Ni and Co, both before and after activation of the Li_2MnO_3 component. To the best of our knowledge, this is the first direct experimental observation that differentiates the reaction kinetics at different transition metal sites in these complex transition metal oxide cathode materials (multiple reaction sites).

2. Results and Discussion

2.1. Material Characterization and Electrochemical Properties

The pristine $Li_{1.2}Ni_{0.15}Co_{0.1}Mn_{0.55}O_2$ material was characterized by XRD, XAS, scanning electron microscopy (SEM), and transmission electron microscopy (TEM). **Figure 1** shows the XRD pattern of the pristine $Li_{1.2}Ni_{0.15}Co_{0.1}Mn_{0.55}O_2$. The pattern presents relatively sharp peaks, indicative of good crystalline

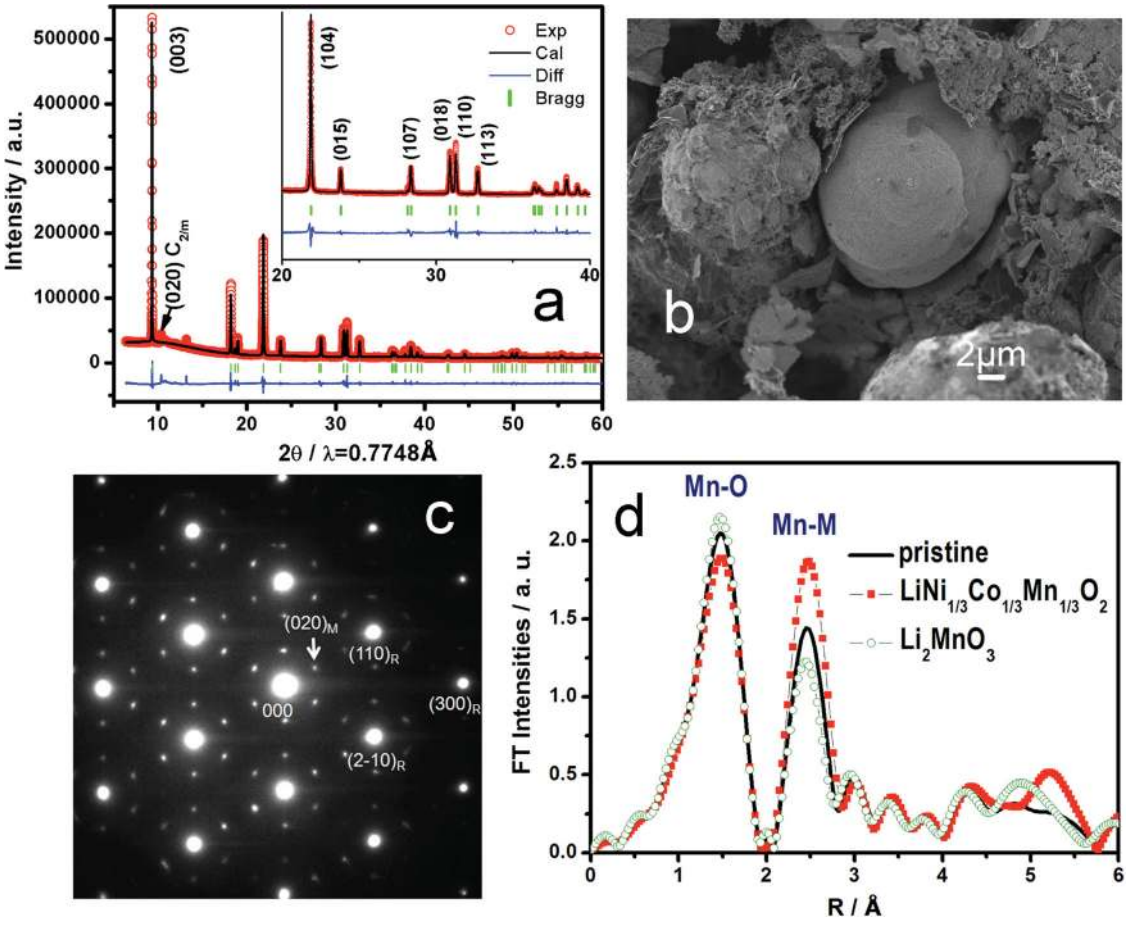

Figure 1. Characterization of pristine $Li_{1.2}Ni_{0.15}Co_{0.1}Mn_{0.55}O_2$ material: a) XRD data, b) SEM image, c) SAED, and d) XAS. All results suggest that the $Li_{1.2}Ni_{0.15}Co_{0.1}Mn_{0.55}O_2$ material can be considered to be a composite integrated with rhombohedral $Li(Ni_{0.375}Co_{0.25}Mn_{0.375})O_2$ and monoclinic Li_2MnO_3 structure domains.

Adv. Energy Mater. 2013,
DOI: 10.1002/aenm.201300950

structure of the material. Most reflections can be indexed in terms of a rhombohedral structure ($R\bar{3}m$, $LiCoO_2$), while a set of weak reflections (around 12°) can be indexed to a monoclinic structure (C2/m, Li_2MnO_3). Figure 1b shows the representative SEM images of the $Li_{1.2}Ni_{0.15}Co_{0.1}Mn_{0.55}O_2$ electrode. It can be observed that the micrometer-sized particles are buried in carbon (graphite and acetylene black) and binder. Selected-area electron diffraction (SAED) presents clear evidence of the coexistence of $LiMO_2$ (M = Ni, Co, Mn) and Li_2MnO_3 domains. The pattern can be considered to be the superposition of a rhombohedral $LiCoO_2$ pattern and three monoclinic Li_2MnO_3 patterns rotated 120° along the [001] axis.[28] Mn extended X-ray absorption fine structure (EXAFS) spectra also confirm that the local environment of Mn absorbers in $Li_{1.2}Ni_{0.15}Co_{0.1}Mn_{0.55}O_2$ is in an intermediate state between $LiNi_{1/3}Co_{1/3}Mn_{1/3}O_2$ and Li_2MnO_3. Overall, the investigated $Li_{1.2}Ni_{0.15}Co_{0.1}Mn_{0.55}O_2$ material can be considered to be a composite integrated by two layered components, $Li(Ni_{0.375}Co_{0.25}Mn_{0.375})O_2$ and $Li(Li_{1/3}Mn_{2/3})O_2$.[29–33] As shown in Supporting Information Figure S1, the K-edge positions for the Mn, Co, and Ni are very close to those of the references Li_2MnO_3 (Mn^{4+}), $LiCoO_2$ (Co^{3+}), and NiO (Ni^{2+}), respectively, suggesting that the oxidation states of the selected absorbing atoms in the pristine sample are close to Mn^{4+}, Co^{3+}, and Ni^{2+}.

To further understand the structure of $Li_{1.2}Ni_{0.15}Co_{0.1}Mn_{0.55}O_2$, aberration-corrected high-angle annular-dark-field scanning transmission electron microscopy (HAADF-STEM) was used to obtain a direct image of the atomic structure (**Figure 2**). The layered components of both Li_2MnO_3 and $LiMO_2$ in the Li-rich layered materials are derived from rhombohedral α-$NaFeO_2$ with Li and M (transition metal ions) occupying the Na and Fe sites, respectively. For Li_2MnO_3, one third of the sites in the transition metal ion plane are replaced by Li to form an ordered $Li_{1/3}Mn_{2/3}$ slab. The $Li_{1/3}Mn_{2/3}$ slabs and the Li interslab layers alternatively stack between the oxygen layers in the C2/m structure. Li_2MnO_3 can also be written as $Li[Li_{1/3}Mn_{2/3}]O_2$ and the [100] zone axis corresponds to the [210] zone axis in $R\bar{3}m$ the space group. The HAADF image of pristine $Li_{1.2}Ni_{0.15}Co_{0.1}Mn_{0.55}O_2$ recorded along the [100] zone axis (based on the C2/m space group) is shown in Figure 2a. Because the image intensity of each atomic column reflects the average atomic number of each atomic column (proportional to $Z^{1.7}$), the bright dots in Figure 2a result from the heavy atomic columns (Ni, Co, and Mn) in $Li_{1.2}Ni_{0.15}Co_{0.1}Mn_{0.55}O_2$, while light atoms are nearly invisible in the image. It can be observed that there are some areas with continuous dots contrast (area I and III) and some other areas with discontinuous dots contrast (area II and IV), as also reflected in the HAADF line profile in Figure 2b. Indeed, $Li_{1/3}(Mn)_{2/3}$ slabs are reflected in the discontinuous areas while the M (transition metal ion) slabs in the $LiMO_2$ component are reflected in the continuous areas. This clearly reveals the coexistence of Li_2MnO_3-like and $LiMO_2$-like areas within the (001) transition metal planes. The domain size of Li_2MnO_3 and $LiMO_2$ with [001] direction is about 2–4 nm. Energy-dispersive X-ray spectroscopy (EDX)-STEM mapping was performed to study the elemental distribution of the pristine $Li_{1.2}Ni_{0.15}Co_{0.1}Mn_{0.55}O_2$ material, the results (Supporting Information Figure S2) further prove the coexistence of the nanosized Li_2MnO_3 and LMO_2 components, and agree well with HAADF observations.

The electrochemical performance of the $Li_{1.2}Ni_{0.15}Co_{0.1}Mn_{0.55}O_2$ material is presented in **Figure 3**. The $Li_{1.2}Ni_{0.15}Co_{0.1}Mn_{0.55}O_2$ electrode was cycled under a current density of 21 mAg^{-1} between 2 V and 4.8 V and the results are shown in Figure 3a,b. A voltage plateau around 4.5 V, which is the typical feature of Li-rich layered materials, can be observed during the first charge. It disappears upon further cycling, indicating an irreversible structure change during the first charge. The capacities obtained for the first charge and discharge are about 320 and 252 mAh g^{-1}, respectively. The irreversible capacity in the first cycle is 68 mAh g^{-1} and

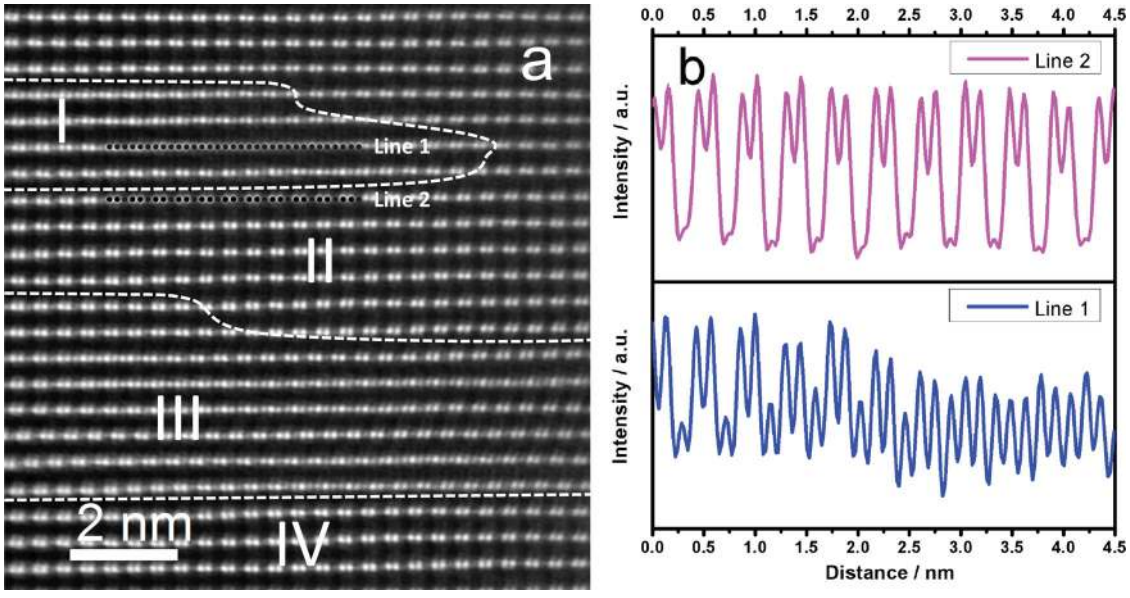

Figure 2. a) HAADF image of pristine $Li_{1.2}Ni_{0.15}Co_{0.1}Mn_{0.55}O_2$ recorded along the [100] zone axis based on C2/m space group, corresponding to the [210] zone axis in the $R\bar{3}m$ space group. b) Line profiles of the HAADF image.

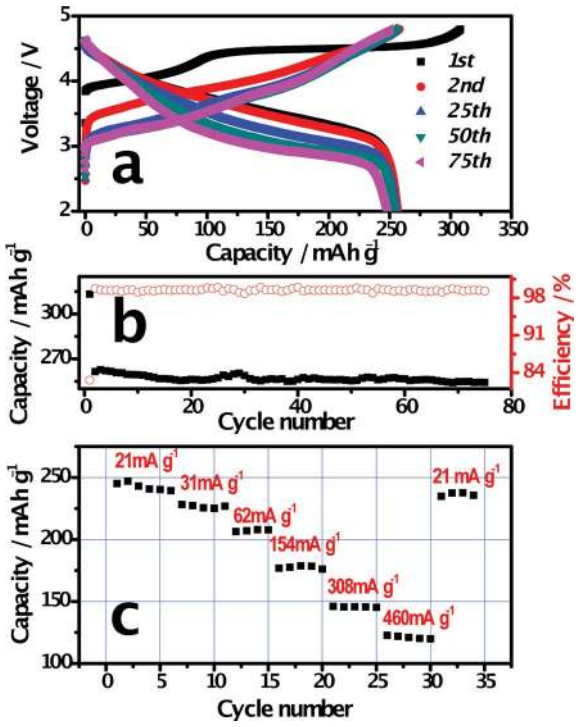

Figure 3. Electrochemical performance of the $Li_{1.2}Ni_{0.15}Co_{0.1}Mn_{0.55}O_2$ material: a) charge–discharge curves at the 1st, 2nd, 25th, 50th, and 75th cycle (current density: 21 mA g^{-1}, 2–4.8 V); b) cyclic performance; and c) rate performance.

the initial efficiency is 79%. The material exhibits very good cyclic performance, and it can be seen that a 248 mAh g^{-1} capacity can be achieved after 75 cycles. The rate performance of the $Li_{1.2}Ni_{0.15}Co_{0.1}Mn_{0.55}O_2$ electrode was also measured (Figure 3c). This shows that the capacity of the $Li_{1.2}Ni_{0.15}Co_{0.1}Mn_{0.55}O_2$ electrode decreases to 120 mAh g^{-1} as the current density increases to 460 mA g^{-1}. The rate performance is poorer than that of the conventional layered cathode materials.[34]

2.2. Characterization of Charge Compensation and Local Structure Evolution During the 1st Cycle and 2nd Charge

To elucidate the changes in the electronic transitions and local structure of the Li-rich layered $Li_{1.2}Ni_{0.15}Co_{0.1}Mn_{0.55}O_2$ material, in situ X-ray absorption spectra at the Mn, Co, and Ni K-edges were collected during the first cycle and second charge under a constant current of 21 mA g^{-1}. **Figure 4**a shows the first charge curve of the $Li_{1.2}Ni_{0.15}Co_{0.1}Mn_{0.55}O_2$/Li cell during in situ XAS experiments. The selected scan numbers of the corresponding XAS spectra are marked on the charge curve. The normalized Mn, Co, and Ni K-edge X-ray absorption near edge structure (XANES) spectra of the $Li_{1.2}Ni_{0.15}Co_{0.1}Mn_{0.55}O_2$ electrode during charge are shown in Figure 4b. In general, the threshold energy position of the K-edge XANES spectra of the transition metals in oxide is sensitive to their oxidation states, while the shape of the peaks is sensitive to the local structural environment of the absorbing element. The K-edge XANES spectra for Ni shown in Figure 4b exhibit the entire rigid edge shift towards higher energy

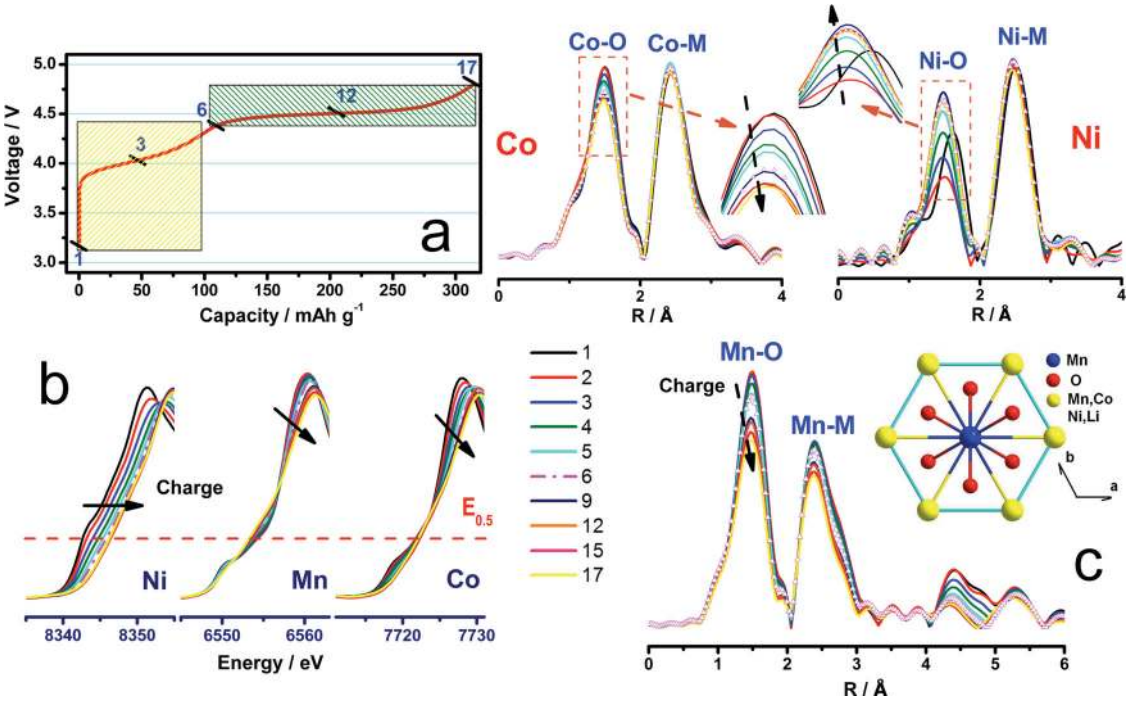

Figure 4. a) The first charging curve of $Li_{1.2}Ni_{0.15}Co_{0.1}Mn_{0.55}O_2$ during an in situ XAS experiment (current density: 21 mA g^{-1}). Selected XAS scan numbers are marked on the charge curves. b) Normalized XANES spectra and c) magnitude of the Fourier transformed Mn, Co, and Ni K-edge spectra of $Li_{1.2}Ni_{0.15}Co_{0.1}Mn_{0.55}O_2$ collected during the initial charge process. Inset: a schematic view of the coordination environment around the transition metal ions.

Adv. Energy Mater. **2013**,
DOI: 10.1002/aenm.201300950

continuously until the charging voltage reaches 4.4 V (scan 6, marked by the dash line), indicating the oxidation of the Ni^{2+} to close to Ni^{4+} in this charging region. Upon further charging to the voltage plateau, only a slight change of the XANES profile can be observed compared to the 4.4 V charged state, with no further change in the K-edge energy position, indicating very little further oxidation of Ni in this voltage range. The interpretation of the Mn and Co K-edge spectral changes in this system is much more complicated. For Mn, the shape of the XANES spectra continuously changes during charging, but the inflection point of the K-edge spectra stays at an almost constant value of approximately 6556 eV throughout the entire charging process, thus implying that the oxidation state of Mn may remain close to Mn^{4+} throughout the charging process. These feature variations of the Mn K-edge at various states of charge are similar to those of conventional layer-structured materials.[35,36] All of the XANES shape changes at the Mn K-edge are caused mainly by the variation of the local structure during Li deintercalation. Similar to the Mn XANES feature, the shape of the Co K-edge spectra continuously changes but the energy position of the absorption edge essentially does not shift at all. Previous work has proposed that the charge compensation for the Li deintercalation process in a similar cathode system could be achieved mainly at both oxygen and cobalt sites simultaneously.[35]

As the K-edge energy position changes of Mn and Co during charge cannot be used to track their contributions to the capacity, in contrast to the case of the Ni K-edge shift, other spectral parameters are needed to correlate the structural changes with the charge capacity contribution of Mn and Co in different charge states. Therefore, we performed EXAFS analysis and correlated the Mn and Co charge capacity with the peak intensity changes of the Mn–O and Co–O first shell obtained by Fourier transform of the K-edge EXAFS spectra and changes in the Debye–Waller factors.

Figure 4c shows the Fourier transformed (FT) EXAFS spectra of Mn, Co, and Ni collected in situ during initial charging. The first peak at around 1.5 Å (it is not phase corrected so the bond length is smaller than the real value) in the FT spectra corresponds to the metal-oxygen interaction in the first coordination sphere, and the second peak at around 2.5 Å is related to the metal-metal interaction in the second coordination sphere, as is labeled in each spectrum and shown in the scheme in Figure 4c. The most significant changes in intensity are observed at the first peak of the metal-oxygen bonding for all Mn, Co, and Ni K-edges during the initial charging process. A closer inspection reveals that the Ni–O and Co–O peaks complete most of their intensity changes when the charging voltage reaches 4.4 V (end of the voltage slope, scan 6, marked by dash line). After that, during further charging through the voltage plateau region, they only exhibit slight changes. In contrast, the Mn-O peak continues its intensity changes in the voltage plateau above 4.4 V all the way to the end of charge at 4.8 V. This suggests that in the voltage slope region (3–4.4 V), the delithiation reaction is mostly related to the oxidation of Ni and Co, while in the voltage plateau region, it is mostly related to the Mn sites during initial charging.

The semiquantitative analysis was performed to elucidate the capacity contributions of Ni, Mn, and Co in different charge (or discharge) states during the first charge, discharge, and the second charge. The results are shown in **Figure 5**. For the

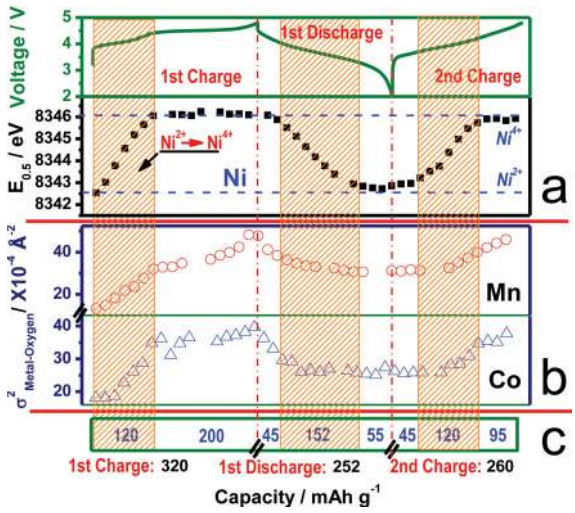

Figure 5. Quantitative correlation of the capacity with the reaction sites. Evolution of a) the half-height energy position of the Ni K-edge XANES spectra and b) Debye–Waller factors of Mn-O and Co-O during in situ XAS measurements. c) The capacity delivered in a corresponding voltage range.

contribution of Ni, the edge position is plotted as a function of charge/discharge states. The half-height energy position was used to indicate the oxidation state of Ni. Upon initial charging, the half energy values gradually increased towards higher values until the charge voltage reached 4.4 V (scan 6), where the edge position moved to a value very close to that corresponding to the oxidation state of Ni^{4+} (using the conventional layered $Li_{1-x}Ni_{1/3}Co_{1/3}Mn_{1/3}O_2$ material for $x > 0.7$ as a reference). The result is shown in Supporting Information Figure S3. The changes in the Mn- and Co- edge position are presented in Supporting Information Figure S4. A capacity of ≈120 mAh g^{-1} was obtained in this voltage range (3–4.4 V) from the charging curve. Based on the Ni content in the sample, 95 mAh g^{-1} could be attributed to the oxidation from Ni^{2+} to Ni^{4+} and the remaining 25 mAh g^{-1} could be attributed to the contribution of Co. It is generally accepted that Co^{3+} ions are partially oxidized to $Co^{3.6+}$,[37] therefore 18 mAh g^{-1} can be attributed to the oxidation of Co^{3+}. The total capacity from oxidation of Ni and Co is 113 mAh g^{-1}, which is slightly smaller than the 120 mAh g^{-1} observed in this voltage range, probably due to the oxygen redox reaction being involved. During the voltage plateau from 4.4 V to 4.8 V, the capacity contribution is mainly attributed to Mn and the contributions from Ni and Co are not accounted for. During first discharge, a 252 mAh g^{-1} capacity was obtained. The Ni K-edge shift started at about 4 V, after 45 mAh g^{-1} capacity had been delivered, and ended at 3.3 V, indicating that the Ni^{4+} to Ni^{2+} reduction mainly occurred in this voltage range. Considering that the capacity contributions from reductions of Ni^{4+} to Ni^{2+} and $Co^{3.6+}$ to Co^{3+} are only 95 mAh g^{-1} and 18 mAh g^{-1}, respectively, calculated from their contents, if the rest of the capacity (i.e., 252 – 95 – 18 = 139 mAh g^{-1}) is only contributed from the reduction of Mn^{4+}, the average oxidation state of Mn should be reduced to $Mn^{3.12+}$ (based on the content of Mn in the sample). Such a big valance change would have been reflected in a significant Mn K-edge shift in the XANES spectra. However, only a very slight Mn

K-edge shift was observed for the discharged electrode compared with the pristine electrode (Supporting Information Figure S5), indicating that other charge compensation mechanisms need to be considered. Based on the recent theoretical calculations for Li_2MnO_3 and the theoretical estimation that the redox potentials are in the order $O^{2-} > Ni^{4+}/Ni^{3+} > Ni^{3+}/Ni^{2+} > Mn^{4+}/Mn^{3+}$,[16,38,39] the capacity contributions can be tentatively assigned to the reaction at oxygen sites for a 4.8–4 V voltage range, and to the reduction of Mn^{4+} for a 3.3–2 V range. During the second charge, the capacity below 3.7 V (before Ni^{2+} oxidation) can be assigned to the contribution of Mn^{3+} to Mn^{4+} oxidation, as proposed by Atsushi et al (in their case of $Li[Ni_{0.17}Li_{0.2}Co_{0.07}Mn_{0.56}]O_2$).[40] The average oxidation state of Mn ions for this sample after the first cycle in the fully discharged state can be estimated as $Mn^{3.74+}$ assuming all of the 45 mAh g^{-1} capacity is contributed by the oxidation of Mn cations to Mn^{4+}. This is slightly higher than the $Mn^{3.6+}$ value reported in ref. [40].

Since the K-edge XANES energy position changes can only be used to track the contribution from Ni, but not Mn and Co, other local structural parameters, namely Debye–Waller factors of the first coordination shells ($\sigma_{Mn\text{-}O}$, $\sigma_{Co\text{-}O}$, and $\sigma_{Ni\text{-}O}$) obtained by fitting the EXAFS equation with model structures,[41] are introduced to track the contributions from Mn and Co during cycling. Theoretically, the value of the Debye–Waller factor reflects the random thermal and static vibration of the absorbing atoms (Mn, Co, and Ni) around their equilibrium atomic positions.[42] A higher degree of local structural disorder that deviates from the ideal model will result in larger values of the Debye–Waller factor.[36] The lithium ion extraction and insertion-induced changes in the local disorder are clearly reflected in the changes in the Debye–Waller factors ($\sigma_{Mn\text{-}O}$, $\sigma_{Co\text{-}O}$, and $\sigma_{Ni\text{-}O}$) and they can therefore be used to track the contributions of Mn and Co.

As shown in Figure 5b, the $\sigma_{Mn\text{-}O}$ values show a continuous increase in the entire voltage range up to 4.8 V during the initial charging process. The changes in these values before the voltage plateau (around 4.5 V) can be caused by the local structure changes induced by the lithium extraction from the $LiMO_2$ structure. The $\sigma_{Co\text{-}O}$ values show significant increase in the first voltage slope region (3–4.5 V). Upon further charging during the voltage plateau region, the $\sigma_{Mn\text{-}O}$ values continue to increase and reach the maximum value at the end of the first charge, while the $\sigma_{Co\text{-}O}$ and $\sigma_{Ni\text{-}O}$ values reveal only a slight change, indicating that the lithium-extraction-induced local structure changes mainly take place around the Mn sites. To distinguish between the contributions from the two different types of structural environments around Mn (the $Li(Ni_{0.375}Co_{0.25}Mn_{0.375})O_2$ part and the $Li(Li_{1/3}Mn_{2/3})O_2$ part), Mn K-edge EXAFS analysis of the the conventional layered $LixNi_{1/3}Co_{1/3}Mn_{1/3}O_2$ was also performed and used as a reference in comparison with $Li_{1.2}Ni_{0.15}Co_{0.1}Mn_{0.55}O_2$ (Supporting Information Figure S6 and Table S1). As can be seen in Figure S6 and Table S1, the decrease of the Mn-O peak intensity for $Li_{1.2}Ni_{0.15}Co_{0.1}Mn_{0.55}O_2$ after delithiation is quite large, but it is almost negligible for $LiNi_{1/3}Co_{1/3}Mn_{1/3}O_2$. In a similar manner, the difference in the $\sigma_{Mn\text{-}O}$ values between pristine ($x = 1.2$) and delithiated ($x = 0.2$) in the $LixNi_{0.15}Co_{0.1}Mn_{0.55}O_2$ sample is three times higher than that between the pristine ($x = 1$) and delithiated material ($x = 0.3$) in the conventional layered $LixNi_{1/3}Co_{1/3}Mn_{1/3}O_2$ (35.1×10^{-4} vs. 8.8×10^{-4}). This indicates that the delithiation-induced local structural changes surrounding Mn in the layered $Li(Ni_{0.375}Co_{0.25}Mn_{0.375})O_2$ part are quite small. Therefore, the severe structural changes in the Mn–O coordination shell observed during the initial delithiation can be mainly attributed to the Li_2MnO_3 components as a result of the elimination of Li/Mn ordering in Li_2MnO_3 and/or the oxygen release accompanied with lithium extraction as observed in lithium-rich layered materials.

In order to investigate this further, in situ XRD patterns were collected during the first charge to observe the long range crystal structure changes in the Li_2MnO_3 component (**Figure 6**).

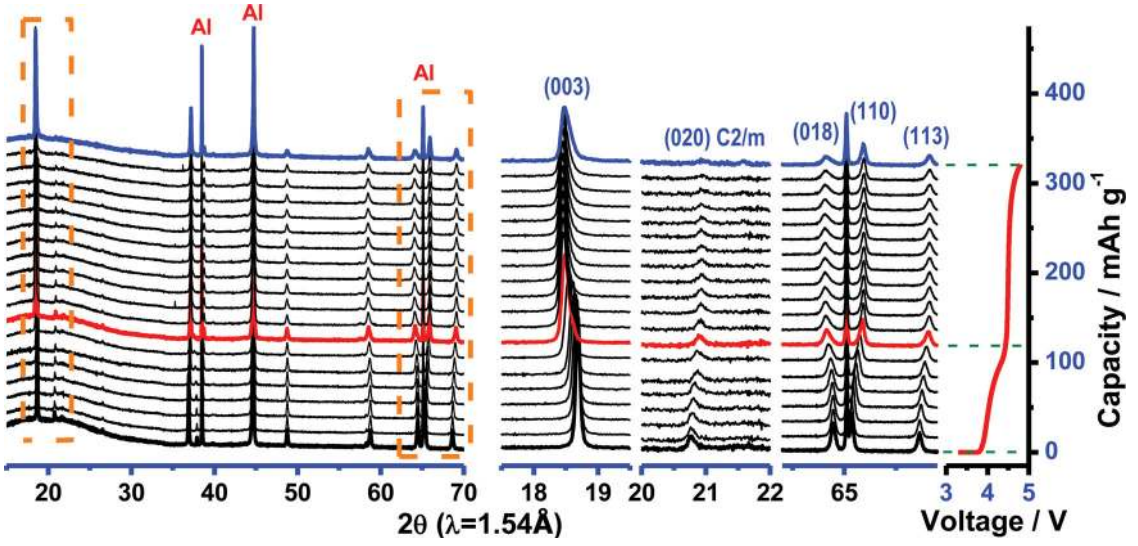

Figure 6. In situ XRD patterns collected during the first charge. The main peaks, which correspond to (003), (018), (110), (113), and $(020)_{C2/m}$, reflections are highlighted in the right column. For easy comparison with the results presented in the literature, the 2θ angle has been converted to values that correspond to the more common laboratory Cu Ka radiation ($\chi = 1.54$ Å). The disappearance of the (020) reflection peaks upon charging to the voltage plateau above 4.5 V is indicative of the disappearance of Li/Mn ordering within the Li_2MnO_3 component.

DOI: 10.1002/aenm.201300950

All major peaks in the XRD patterns can be indexed by the α-$NaFeO_2$ structure with the $R\bar{3}m$ space group for the pristine material, except for a peak in lower angle region (20–21°), which can be indexed as (020) with the C2/m space group. This is due to the Li/Mn ordering in the transition metal layer and is indicative of the presence of the Li_2MnO_3 components. Before the voltage plateau was reached, the typical structure evolution features of the conventional layered material can be observed, with the (003) peak shift to lower angles reflecting an increased lattice parameter "*c*" due to the increased repulsion between the oxygen layers with a simultaneous (110) peak shift to the higher angles caused by the decrease in the average metal–metal distance due to oxidation of Ni^{2+} and Co^{3+}. Most of the decrease in the intensity of the superlattice peak (020) during the first charge took place only in the voltage plateau (4.5–4.8 V) region. This suggests that the loss of the Li/Mn ordering in Li_2MnO_3 component occurs most in this region.[10,11,19,43] This is in good agreement with the XAS results, which revealed that the local structural changes mainly occurred near Mn sites in the Li_2MnO_3 component during initial charging in the voltage plateau region. The Li/Mn ordering was not recovered during subsequent cyclings (Supporting Information Figure S7), indicating the irreversible structure changes after the initial delithiation process. This is in good agreement with the relative large $\sigma_{Mn\text{-}O}$, $\sigma_{Co\text{-}O}$, and $\sigma_{Ni\text{-}O}$ values throughout the first discharge and second charge. This is further supported by the HRTEM images, as shown in **Figure 7**. The cycled material shows regions with highly degraded (003) lattice fringes randomly distributed on the nanoscale. The degradation can be considered to be a consequence of the irreversible local structure changes within the Li_2MnO_3 component after the initial delithiation process and/or the O_2 evolution from the Li_2MnO_3 components a shas been discussed previously.[44]

The proposed charge compensation mechanisms of the investigated $Li_{1.2}Ni_{0.15}Co_{0.1}Mn_{0.55}O_2$ material are summarized in **Table 1**. The reaction mechanisms are based on the analysis of both the K-edge XANES and EXAFS spectra and the theoretically estimated redox potentials of the transition metal ions. Oxidation of the Ni^{2+} and the reaction at the Co site contribute a combined 113 mAh g^{-1} capacity in the voltage slope region (3–4.4 V, total capacity is 120 mAh g^{-1} in this voltage range), while the reaction of Li_2MnO_3 component in the plateau region (4.5–4.8 V) contributes 200 mAh g^{-1} capacity during the first charge process. For the first discharge, before reduction of Ni^{4+} (4.8–4 V), 45 mAh g^{-1} capacity could be attributed to the charge compensation of oxygen. After the 113 mAh g^{-1} contribution from the reduction of Ni^{4+} to Ni^{2+} and $Co^{3.6+}$ to Co^{3+} (4–3.3 V), the reaction in the low voltage region (3.3–2 V) can be attributed to the reduction of Mn^{4+} ions. During the second charge, the charge compensation process shows the similar behavior as the first discharge process but in a reversed direction. The large variance of the Debye–Waller factor, $\sigma_{Mn\text{-}O}$, further supports that the severe local structure changes occurred in the Li_2MnO_3 regions. The relatively large $\sigma_{Mn\text{-}O}$, $\sigma_{Co\text{-}O}$, and $\sigma_{Ni\text{-}O}$ values after the first cycle (compared to the pristine sample) indicate the irreversible structure changes after the initial activation process. In addition, the local structure parameter values of $\sigma_{Mn\text{-}O}$, $\sigma_{Co\text{-}O}$, and $\sigma_{Ni\text{-}O}$ associated with the local structure disordering are correlated with the lithium content (capacity) in a semi-quantitative way. They will be used to estimate the delithiated extent during constant voltage charge.

Table 1. Charge compensation mechanism of the $Li_{1.2}Ni_{0.15}Co_{0.1}Mn_{0.55}O_2$ during the first cycle and second discharge process.

	Mn^{3+}- Mn^{4+}	Ni^{2+}- Ni^{4+} and Co^{3+}- $Co^{3.6+}$	Mn^{4+}-O^{2-x}
1st charge	–	3–4.4 V: 113 mAh g^{-1}	4.4–4.8 V: 200 mAh g^{-1}
1st discharge	3.3–2 V: 55 mAh g^{-1}	4–3.3 V: 113 mAh g^{-1}	4.8–4 V: 45 mAh g^{-1}
			4–3.3 V: 39 mAh g^{-1}
2nd charge	2–3.7 V: 45 mAh g^{-1}	3.7–4.2 V: 113 mAh g^{-1}	4.2–4.8 V: 95 mAh g^{-1}

2.3. Reaction Polarization and its Structural Origin

The polarization behavior during charge is strongly related to the reaction kinetics. The galvanostatic intermittent titration technique (GITT) was used to study the reaction kinetics of pristine and cycled samples at various states of charge,[45] which can be linked to certain charge compensation mechanisms. When the GITT technique is used, the cell is charged by a constant current (CC) at 21 mA g^{-1} for 1 h and then relaxed by cutting off the current for 12 h to reach a near-equilibrium state; this process is then repeated until the final cut-off voltage value is reached. The results for the first and firth charge are plotted in **Figure 8**. The voltage difference between the end of each interrupted CC charge and the end of relaxation, defined as the overpotential,[46] can be used as an indicator of the kinetics: the larger the overpotential, the poorer the kinetics. The regions assigned to different charge compensation mechanisms according to the XAS and XRD results and theoretical calculations are marked in Figure 8 using horizontal dashed-dotted lines as boundaries.

It can be seen in Figure 8a during the first charge that the overpotential values remained

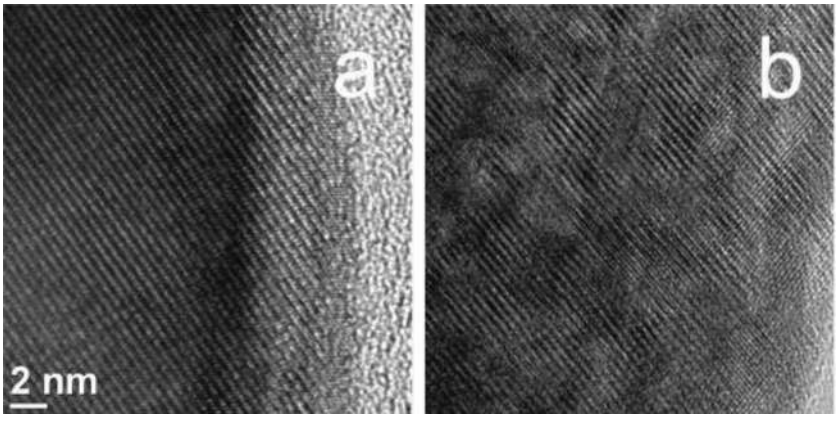

Figure 7. HRTEM images of a) pristine and b) five-times cycled $Li_{1.2}Ni_{0.15}Co_{0.1}Mn_{0.55}O_2$. Irreversible structure changes can be observed locally after cycling.

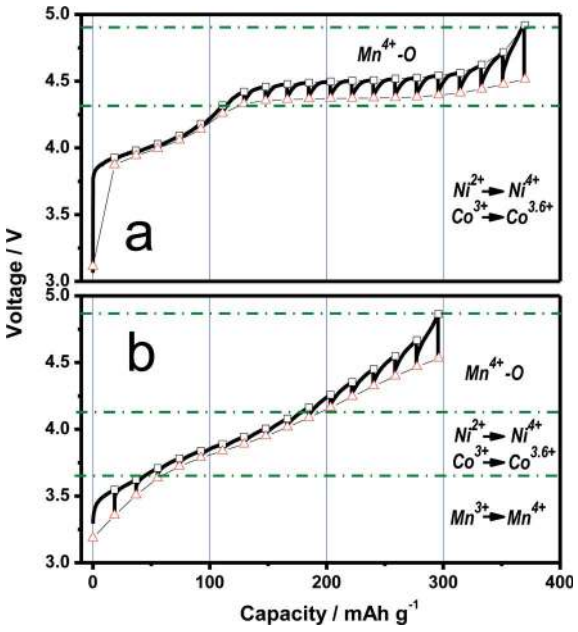

Figure 8. GITT curves of the $Li_{1.2}Ni_{0.15}Co_{0.1}Mn_{0.55}O_2$ electrode for Li extraction obtained during a) the first charge and b) the fifth charge. Solid line: GITT result; dashed line: open-circuit voltage curve. The regions assigned to different charge compensation mechanisms according to the XAS results are marked using horizontal dashed-dotted lines as boundaries. The reaction related to Mn shows the poorer kinetics compared to Ni and Co.

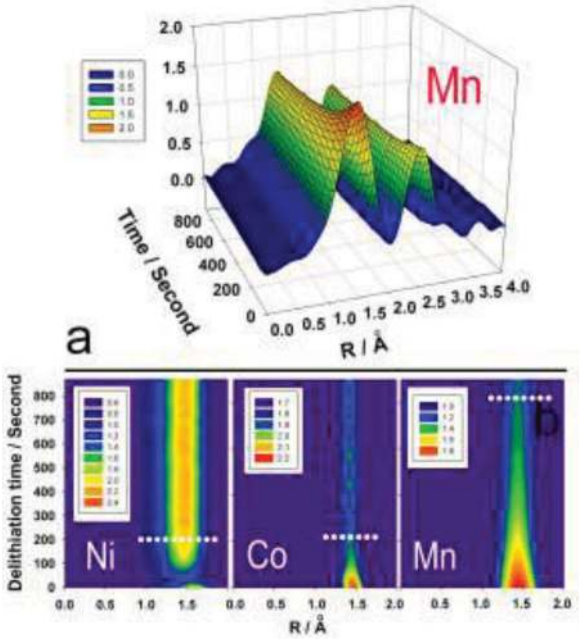

Figure 9. 5 V constant voltage charging was applied on the $Li_{1.2}Ni_{0.15}Co_{0.1}Mn_{0.55}O_2$ electrode. Ni, Co, Mn reacted simultaneously, which was recorded using a time-resolved XAS technique. a) Magnitude of the Fourier transformed Mn K-edge spectra of $Li_{1.2}Ni_{0.15}Co_{0.1}Mn_{0.55}O_2$ collected during 5 V constant voltage charging. b) Projection view of the corresponding Ni–O, Co–O, and Mn–O peak magnitudes of the Fourier transformed K-edge spectra as functions of charging time.

low in the voltage range between 3 V and 4.3 V, where the charge compensation is mainly attributed to the oxidation of Ni^{2+} and Co^{3+} showing the best kinetic region. In contrast, the higher values of the polarization in the voltage range between 4.5 V and 4.8 V, where the charge compensation is believed to be mainly in Li_2MnO_3, exhibit much more sluggish reaction kinetics compared to those in the $Li(Ni_{0.375}Co_{0.25}Mn_{0.375})O_2$ component regions for the initial activation process.

The results in Figure 8b for the fifth charge show a slight decrease in the average reaction overpotential in the corresponding Mn reaction regions (2–3.7 V and 4.2–4.8 V), compared with the initial charge. This delithiation kinetic difference is understandable due to the irreversible structure change after the initial delithiation process in the Li_2MnO_3 regions. Moreover, the average reaction overpotential value is still larger than that in the Ni and Co reaction regions, further indicative of the different charge compensation mechanisms at the corresponding Ni/Co and Mn sites and their structure origins.

2.4. Element-Dependent Kinetic Behavior

To study the elementally dependent delithiation kinetics, XAS spectra were collected in situ during a 5-V constant-voltage charge. The applied voltage is higher than all of the redox potentials for Ni^{2+}/Ni^{3+}, Ni^{3+}/Ni^{4+}, Co^{3+}/Co^{4+} and the activation voltage of Li_2MnO_3, therefore the delithiation reaction related to Ni, Co, and Mn can be probed simultaneously. In order to capture the quick changes in the XAS spectra, a time-resolved XAS technique was used to dynamically monitor the delithiation process. The time-resolved XAS technique using a monochrometer in continuous motion mode with constant velocity to replace the stepwise scanning mode used in conventional XAS has the advantages of collecting one spectrum in less than one second. The data collection time for each spectrum was optimized to be 15 s to balance the signal-to-noise ratio and the number of spectra collected.

Figure 9a shows the 3D Fourier transformed magnitude of the Mn K-edge EXAFS spectra collected during 5 V constant voltage for the pristine electrode. The most significant change is in the first coordination shell (Mn–O) around the Mn atoms. The decrease of the first coordination shell peak intensities during 5 V constant voltage charge is similar to that observed during constant current charge, indicating that the local structure changes around the Mn sites are caused by Li^+ extraction. The comparative Fourier transformed magnitude of the corresponding Ni, Co, and Mn K-edge EXAFS spectra during constant voltage charge for a total time of 900 s are plotted in a 2D view (Figure 9b), using a color scale for the spectral intensity. For Ni, the first coordination peaks (Ni–O) show dramatic changes in both position and intensity within the first 100 s, which represents that the charge compensation occurred at the Ni sites. The peak intensities decreased first (from 0 s to ≈60 s) due to the aforementioned Jahn–Teller distortion caused by the oxidation of Ni^{2+} to Ni^{3+},[47,48] then turned around to increase with further oxidation of Ni^{3+} to Ni^{4+}. The EXAFS features remain unchanged after 160 s, indicating that the oxidation of

DOI: 10.1002/aenm.201300950

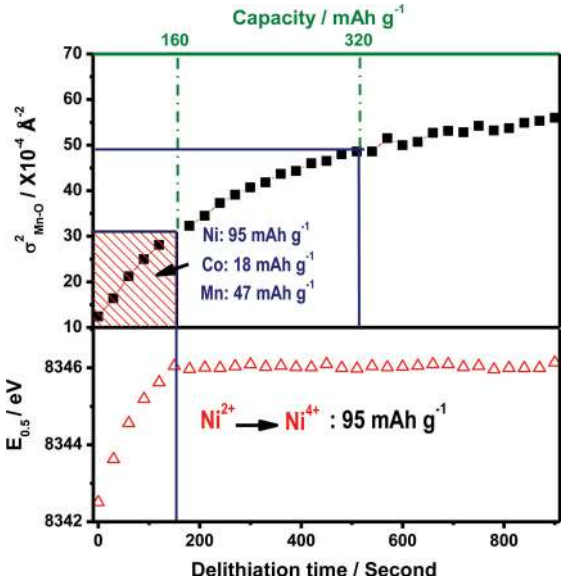

Figure 10. A quasi-quantitative analysis of the delithiation process of the $Li_{1.2}Ni_{0.15}Co_{0.1}Mn_{0.55}O_2$ electrode during 5 V constant voltage charging. The capacities delivered from Ni and Co are based on their content in the material; the total capacity is estimated from the $\sigma_{Mn\text{-}O}$ value that is associated with the extracted lithium content. The correlation between the $\sigma_{Mn\text{-}O}$ value and the lithium content (capacity) has been identified, as discussed for the in situ constant current cycling.

Ni^{2+} to Ni^{4+} was almost completed within the first 3 min. Compared to Ni, the evolution of the local structure around the Co and Mn sites caused by Li^+ extraction are more straightforward, as displayed in Figure 9b: the first coordination shell peak (Co–O and Mn–O) intensities show a continuous decrease. No obvious Co–O peak intensity changes can be observed after 200 s at 5 V charge while the Mn–O peak intensities continued to decrease over the entire observation time scale (900 s), indicating much slower delithiation kinetics around the Mn sites.

To further determine the reaction dynamic difference between each element, quantitative analysis similar to that applied for in situ constant current cycling was performed for this 5 V constant voltage charge. Assuming the structural transformation undergoes a similar pathway during Li^+ extraction for both constant current and constant voltage charging, the structural parameters extracted from fitting the XAS spectra collected during in situ constant current charge were used to identify the delithiation states during constant voltage charge. The Debye–Waller factor $\sigma_{Mn\text{-}O}$ values obtained at constant charge were correlated with the Li content (specific capacity) of the sample and used to identify the delithiation level during constant voltage charge. As shown in **Figure 10**, the Debye–Waller factor $\sigma_{Mn\text{-}O}$ values for Mn continue to increase for the entire 900 s time scale (leveling off after 500 s), indicating a continuous structure change caused by lithium extraction. The $\sigma_{Mn\text{-}O}$ at t = 500 s is equal to the value of constant current charge at 4.8 V. This implies that under 5 V constant voltage charging for 500 s, lithium can be extracted to the level equal to the constant current charge (21 mA g^{-1}) at 4.8 V, where a 320 mAh g^{-1} capacity was obtained. In order to verify the validity of this correlation, the FT-EXAFS spectra of Mn K-edge for constant current charge (21 mA g^{-1}) at 4.8 V and the spectra for 5 V constant voltage charge after 500 s with the same $\sigma_{Mn\text{-}O}$ values are plotted in Supporting Information Figure S8 (as well as the constant current charge at 4.5 V and constant voltage charge after 160 s). The perfect match of these two curves verified that using the $\sigma_{Mn\text{-}O}$ values to indicate the content of Li during delithiation is valid. After 500 s, although lithium can be further extracted near Mn site, the rate is significantly slowed down, as indicated by the leveling off of the $\sigma_{Mn\text{-}O}$ values. The changes of the half-height energy of Ni K-edge XANES spectra as a function of delithiation time are presented in the bottom part of Figure 10. The oxidation of Ni^{2+} to Ni^{4+} was almost completed in 160 s where it delivers 95 mAh g^{-1} capacity (based on the Ni content in the material). Considering the total delivered capacity estimated from the $\sigma_{Mn\text{-}O}$ value is 160 mAh g^{-1} and assuming the oxidation of Co^{3+} contributes 18 mAh g^{-1} capacity (based on Co content in material) within this first 160 s, the rest of the capacity contributed from the Mn sites is only 47 mAh g^{-1}. Comparing to the estimated total capacity of 207 mAh g^{-1} from the Mn contribution at 500 s (i.e., 320 – 95 – 18), this 47 mAh g^{-1} is a very small portion of it. This indicates that the delithiation kinetics at the Mn sites (mostly likely in the Li_2MnO_3 component) are much poorer than at the Ni and Co sites. However, it is still surprising that Li^+ can be extracted from Li_2MnO_3 in such a short period of time (500 s) because well-crystallized pure Li_2MnO_3 was considered to be electrochemically inactive. The electrochemical activity of Li_2MnO_3 is due to the extremely small (nanodimensional) size of the Li_2MnO_3 domains, which are distributed randomly throughout the composite structure as was confirmed by the HAADF-STEM results. The nanosized features of Li_2MnO_3 facilitate the lithium diffusion and extraction with a concomitant oxygen release.

The delithiation kinetic difference between pristine and cycled electrodes was also investigated and is presented in **Figure 11** for Mn and Ni, respectively. The corresponding results for Co are shown in Supporting Information Figure S9. The cycled electrode was prepared by pre-cycling the pristine electrode under constant current in a voltage range from 2 V to 4.8 V for five cycles. Therefore, the activation process of the Li_2MnO_3 component can be considered to be sufficiently completed. For Ni, the lithium extraction with a concomitant oxidation of the divalent nickel ions to the tetravalent state reveals a very similar kinetic feature for both pristine and cycled electrodes, as shown in Figure 11a. In contrast, the reaction kinetic behavior at the Mn sites shows a significant improvement for the cycled electrode, indicated by the flat $\sigma_{Mn\text{-}O}$ values after 500 s. This is also consistent with the GITT observation (Figure 8). However, the delithiation kinetics in the Mn regions for the cycled electrode are still poorer than those in the Ni regions, indicating that the delithiation kinetics of this material are limited by the reaction around the Mn sites.

2.5. General Discussion of the Optimization of High-Rate Performance Li-Rich Layered Materials

Our studies of GITT and time-resolved XAS during constant voltage charging at 5 V showed clearly that the poor delithiation kinetics are closely related to the Mn sites (more likely

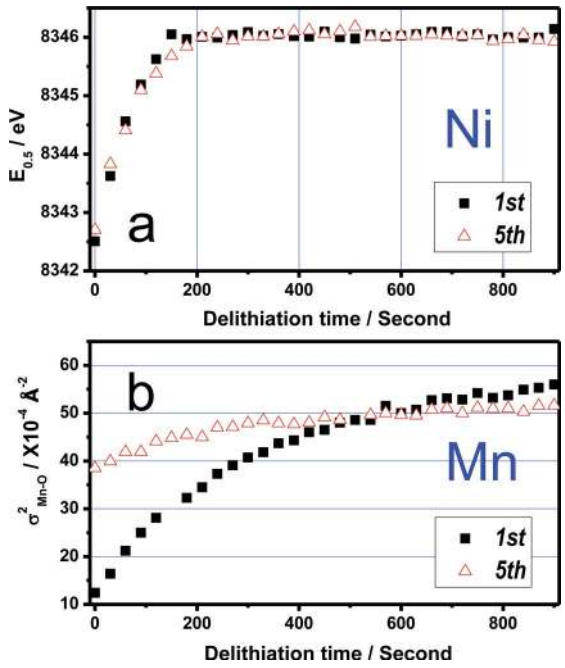

Figure 11. Comparison of the delithiation kinetics of the pristine and cycled $Li_{1.2}Ni_{0.15}Co_{0.1}Mn_{0.55}O_2$ electrodes under constant voltage charging: a) Ni and b) Mn. The Mn sites reveal poorer delithiation kinetics compared to Ni, even after initial activation of the Li_2MnO_3 component.

in the Li_2MnO_3 component) of $xLiMO_2(1-x)Li_2MnO_3$ materials caused by the disordered structure formed during and after the activation of the Li_2MnO_3 component. Therefore, the Li_2MnO_3 component is the key limiting factor for the relatively poor rate capability of these materials. In contrast, the Ni and Co related to fast delithiation kinetics are not negatively affected very much by the activation process. The possible reasons for the sluggish kinetics of the Mn-related sites are migration of Mn,[43] oxygen release, and oxygen redox reaction. Because the Li_2MnO_3 is the essential component for these high-energy-density cathode materials, the right strategy for improving the rate capability of these materials would be optimizing the properties of Li_2MnO_3 (minimizing the content, stabilizing the Mn lattice, and doping) to balance the energy density and rate capability and to meet the requirements for different applications.

3. Conclusions

The structure of the Li-rich layered $Li_{1.2}Ni_{0.15}Co_{0.1}Mn_{0.55}O_2$ cathode material has been studied using XRD, XAS, and TEM techniques. The results indicate that the $Li_{1.2}Ni_{0.15}Co_{0.1}Mn_{0.55}O_2$ material is a composite formed by conventional layered $LiMO_2$ (M = Ni, Co, Mn) and Li_2MnO_3 components. The aberration-corrected HAADF-STEM image provides direct evidence that $LiMO_2$- and Li_2MnO_3-like domains coexist with 2–4 nm size. The structural changes and charge compensation mechanisms for each $LiMO_2$ and Li_2MnO_3 component during lithium extraction and insertion have been studied using in situ XRD and XAS experiments. It is observed that a portion of the capacity can be attributed to the Li_2MnO_3 component, resulting in a large reversible capacity of the Li-rich layered materials in addition to the capacity contributed by the Ni and Co redox reactions. However, the delithiation kinetics features revealed using a time-resolved XAS technique indicate much poorer delithiation kinetics in the Mn-related process (mostly in the Li_2MnO_3 component), compared to faster reaction kinetics for Ni and Co, which are only minimally affected in a negative way by the irreversible structure change of the Li_2MnO_3 component after the initial delithiation process. The major source for the slow reaction kinetics was identified in this work as being the Li_2MnO_3 component. A new approach for designing and improving Li-rich layered cathode materials with better reaction kinetics may be provided by tailoring the Li_2MnO_3 component. In addition, the novel time-revolved technique and analysis method used in this study can also be applied to investigate the reaction kinetics of other lithium-ion battery materials and other battery systems.

4. Experimental Section

Material Characterization: The $Li_{1.2}Ni_{0.15}Co_{0.1}Mn_{0.55}O_2$ synthesized at Argonne National Laboratory, was analyzed by SEM (JEOL 7600F) and TEM (JEOL JEM-2100F). High-quality XRD patterns were collected in transmission mode at beamline X14A of NSLS (USA) using a linear position sensitive silicon detector. The wavelength used was 0.7748 Å.

Aberration-corrected HAADF-STEM and EDX-STEM were performed using a JEOL ARM 200F (JEOL, Tokyo, Japan) TEM operated at 200 keV. The attainable spatial resolution of the microscope was 80 pm at an incident angle of 40 mrad. The Ni–K, Co–K, and Mn–K edges were used to collect chemical information for the individual elements.

Electrochemical Cells: The $Li_{1.2}Ni_{0.15}Co_{0.1}Mn_{0.55}O_2$ cathode electrodes were prepared by slurring the active material, carbon black, and polyvinylidenefluoride (PVDF) with a weight ratio of 86:6:8 in *n*-methyl pyrrolidone (NMP) solvent, then coating the mixture onto an Al foil. High-purity lithium foil was used as the anode. The electrolyte was 1.2 m $LiPF_6$ in ethylene carbonate (EC) and dimethyl carbonate (DMC) solvent (3:7 by volume, Novolyte Inc.). The 2032-type button cells for electrochemical studies were assembled in an argon-filled glove box and tested on a VMP3 BioLogic electrochemistry workstation. GITT experiments (Biologic Inc) were performed by charging/discharging the cell for 1 h at a current density of 21 mA g^{-1} and relaxing for 12 h to reach a quasi-equilibrium state and then repeating this process until the voltage limitation was reached.

X-Ray Absorption Spectroscopy: Hard XAS experiments were carried out at beamline X18A of the National Synchrotron Light Source (NSLS) at Brookhaven National Laboratory. Both conventional and time-resolved in situ XAS experiments were performed in transmission mode using a Si (111) double-crystal monochromator detuned to 35–45% of its original maximum intensity to eliminate the high order harmonics. A reference spectrum for each element was simultaneously collected with the corresponding spectrum of the in situ cells using transition metal foil. Energy calibration was carried out using the first inflection point of the K-edge spectrum of transition metal foil as reference (i.e., Ni: 8333 eV). XANES and EXAFS data were analyzed using the ATHENA software package.[49]

Supporting Information

Supporting Information is available from the Wiley Online Library or from the author.

DOI: 10.1002/aenm.201300950

Acknowledgements

The authors thank Dr. Daniel Abraham at Argonne National Laboratory for providing the samples. This work was supported by the U.S. Department of Energy, the Assistant Secretary for Energy Efficiency and Renewable Energy, Office of Vehicle Technologies under Contract Number DE-AC02-98CH10886 for BNL and Contract No. DE-AC02-06CH11357 for ANL. This work at IOP, CAS was funded by CAS Innovation project (KJCX2-YW-W26) and "973" project (2012CB932900). The authors acknowledge technical support from the beamline scientists at X14A, X18A, X19A (NSLS, BNL) and 11-BM-B at APS (APS, ANL).

Received: August 1, 2013
Revised: September 10, 2013
Published online:

[1] Z. Lu, J. R. Dahn, *J. Electrochem. Soc.* **2002**, *149*, 815.
[2] Z. Lu, D. D. MacNeil, J. R. Dahn, *Electrochem. Solid-State Lett.* **2001**, *4*, A191.
[3] S. H. Kang, Y. K. Sun, K. Amine, *Electrochem. Solid-State Lett.* **2003**, *6*, A183.
[4] C. P. Grey, W. S. Yoon, J. Reed, G. Ceder, *Electrochem. Solid-State Lett.* **2004**, *7*, A290.
[5] M. M. Thackeray, C. S. Johnson, J. T. Vaughey, N. Li, S. A. Hackney, *J. Mater. Chem.* **2005**, *15*, 2257.
[6] M. M. Thackeray, S. H. Kang, C. S. Johnson, J. T. Vaughey, R. Benedek, S. A. Hackney, *J. Mater. Chem.* **2007**, *17*, 3112.
[7] H. J. Yu, H. S. Zhou, *J. Mater. Chem.* **2012**, *22*, 15507.
[8] Y. K. Sun, M. J. Lee, C. S. Yoon, J. Hassoun, K. Amine, B. Scrosati, *Adv. Mater.* **2012**, *9*, 1192.
[9] A. R. Armstrong, M. Holzapfel, P. Novak, C. S. Johnson, S. H. Kang, M. M. Thackeray, P. G. Bruce, *J. Am. Chem. Soc.* **2006**, *128*, 8694.
[10] N. Tran, L. Croguennec, M. Menetrier, F. Weill, Ph. Biensan, C. Jordy, C. Delmas, *Chem. Mater.* **2008**, *20*, 4815.
[11] N. Yabuuchi, K. Yoshii, S. T. Myung, I. Nakai, S. Komaba, *J. Am. Chem. Soc.* **2011**, *133*, 4404.
[12] Y. Wu, A.V. Murugan, A. Manthiram, *J. Electrochem. Soc.* **2008**, *155*, A635.
[13] Y. Wu, A. Manthiram, *Solid State Ionics* **2009**, *180*, 50.
[14] C. R. Fell, D. Qian, K. J. Carroll, M. F. Chi, J. L. Jones, Y. S. Meng, *Chem. Mater.* **2013**, *25*, 1621.
[15] T. Ohzuku, M. Nagayama, K. Tsuji, K. Ariyoshi, *J. Mater. Chem.* **2011**, *21*, 10179.
[16] R. J. Xiao, H. Li, L. Q. Chen, *Chem. Mater.* **2012**, *24*, 4242.
[17] A. D. Robertson, P. G. Bruce, *Electrochem. Solid-State Lett.* **2004**, *7*, A294.
[18] P. Kalyani, S. Chitra, T. Mohan, S. Gopukumar, *J. Power Sources* **1999**, *80*, 103.
[19] M. Jiang, B. Key, Y. S. Meng, C. P. Grey, *Chem. Mater.* **2009**, *21*, 2733.
[20] Q. Y. Wang, J. Liu, A. V. Murugan, A. Manthiram, *J. Mater. Chem.* **2009**, *19*, 4965.
[21] B. Xu, C. R. Fell, M. Chi, Y. S. Meng, *Energy Environ. Sci.* **2011**, *4*, 2223.
[22] J. Li, R. Klopsch, M. C. Stan, S. Nowak, M. Kunze, M. Winter, S. Passerini, *J. Power Sources* **2011**, *196*, 4821.
[23] H. J. Yu, Y. R. Wang, D. Asakura, E. Hosono, H. S. Zhou, *RSC Adv.* **2012**, *2*, 8797.
[24] A. D. Robertson, P.G. Bruce, *Chem. Mater.* **2003**, *15*, 1984.
[25] D. Y. W. Yu, K. Yanagida, Y. Kato, H. Nakamura, *J. Electrochem. Soc.* **2009**, *44*, 5579.
[26] F. Amalraj, B. Markovsky, D. Sharon, M. Talianker, E. Zinigrad, R. Persky, O. Haik, J. Grinblat, J. Lampert, M. Schulz-Dobrick, A. Garsuch, L. Burlaka, D. Aurbach, *Electrochim. Acta* **2012**, *78*, 32.
[27] X. Q. Yu, Q. Wang, Y. N. Zhou, H. Li, X. Q. Yang, K. W. Nam, S. N. Ehrlich, S. Khalid, Y. S. Meng, *Chem. Commun.* **2012**, *48*, 11537.
[28] J. Bareno, M. Balasubramanian, S. H. Kang, J. G. Wen, C. H. Lei, S. V. Pol, I. Petrov, D. P. Abraham, *Chem. Mater.* **2011**, *23*, 2039.
[29] C. S. Johnson, J. S. Kim, C. Lefief, N. Li, J. T. Vaughey, M. M. Thackeray, *Electrochem. Commun.* **2004**, *6*, 1085.
[30] M. M. Thackeray, S. H. Kang, C. S. Johnson, J. T. Vaughey, S. A. Hackney, *Electrochem. Commun.* **2006**, *8*, 1531.
[31] J. Bareno, C. H. Lei, J. G. Wen, S. H. Kang, I. Petrov, D. P. Abraham, *Adv. Mater.* **2010**, *22*, 1122.
[32] A. Boulineau, L. Simonin, J. F. Colin, E. Canévet, L. Daniel, S. Patoux, *Chem. Mater.* **2012**, *24*, 3558.
[33] H. J. Yu, R. Ishikawa, Y. G. So, N. Shibata, T. Kudo, H. S. Zhou, Y. Ikuhara, *Angew. Chem. Int. Ed.* **2013**, *52*, 1.
[34] S. L. Wu, W. Zhang, X. Y. Song, A. K. Shukla, G. Liu, V. Battaglia, V. Srinivasan, *J. Electrochem. Soc.* **2012**, *159*, A438.
[35] W. S. Yoon, M. Balasubramanian, K. Y. Chung, X. Q. Yang, J. McBreen, C. P. Grey, D. A. Fischer, *J. Am. Chem. Soc.* **2005**, *127*, 17479.
[36] Y. W. Tsai, B. J. Hwang, G. Ceder, H. S. Sheu, D. G. Liu, J. F. Lee, *Chem. Mater.* **2005**, *17*, 3191.
[37] T. A. Arunkumar, Y. Wu, A. Manthiram, *Chem. Mater.* **2007**, *19*, 3067.
[38] J. Song, D. W. Shin, Y. H. Lu, C. D. Amos, A. Manthiram, J. B. Goodenough, *Chem. Mater.* **2012**, *24*, 3101.
[39] J. B. Goodenough, Y. Kim, *Chem. Mater.* **2010**, *22*, 587.
[40] A. Itoa, Y. Satob, T. Sanadac, M. Hatanoa, H. Horiea, Y. Ohsawaa, *J. Power Sources* **2011**, *196*, 6828.
[41] D. E. Sayers, E. A. Stern, F. W. Lytle, *Phys. Rev.Lett.* **1971**, *27*, 1204.
[42] J. J. Rehr, R. C. Albers, *Rev. Mod. Phys.* **2000**, *72*, 621.
[43] R. Wang, X. Q. He, L. H. He, F. W. Wang, R. J. Xiao, L. Gu, H. Li, L. Q. Chen, *Adv. Energy Mater.* **2013**, *3*, 1358.
[44] K. S. Park, A. Benayad, M. S. Park, W. Choi, D. Im, *Chem. Commun.* **2010**, *46*, 4190.
[45] W. Weppner, R. A. Huggins, *J. Electrochem. Soc.* **1977**, *124*, 1569.
[46] J. P. Sun, K. Tang, X. Q. Yu, H. Li, X. J. Huang, *Solid State Ionics* **2008**, *179*, 2390.
[47] I. Nakai, K. Takahashi, Y. Shiraishi, T. Nakagome, F. Izumi, Y. Ishii, F. Nishikawa, T. Konishi, *J. Power Sources* **1997**, *68*, 536.
[48] A. Demourgues, L. Gautier, A. V. Chadwick, C. Delmas, *Nucl. Instrum. Methods Phys. Res.* **1997**, *133*, 39.
[49] B. Ravel, M. Newville, *J. Synchrotron Radiat.* **2005**, *12*, 537.